

A 2.5-mm diameter probe for photoacoustic and ultrasonic endoscopy

Joon-Mo Yang,^{1,3} Ruimin Chen,^{2,3} Christopher Favazza,¹ Junjie Yao,¹ Chiye Li,¹ Zhilin Hu,¹ Qifa Zhou,^{2,4} K. Kirk Shung,² and Lihong V. Wang^{1,*}

¹Optical Imaging Laboratory, Department of Biomedical Engineering, Washington University in St. Louis, Campus Box 1097, One Brookings Drive, St. Louis, Missouri 63130, USA

²NIH Ultrasonic Transducer Resource Center, Department of Biomedical Engineering, University of Southern California, 1042 Downey Way, University Park, DRB 130, Los Angeles, California 90089, USA

³These authors contributed equally to this work

⁴qifazhou@usc.edu

*lhwang@biomed.wustl.edu

Abstract: We have created a 2.5-mm outer diameter integrated photoacoustic and ultrasonic mini-probe which can be inserted into a standard video endoscope's instrument channel. A small-diameter focused ultrasonic transducer made of PMN-PT provides adequate signal sensitivity, and enables miniaturization of the probe. Additionally, this new endoscopic probe utilizes the same scanning mirror and micromotor-based built-in actuator described in our previous reports; however, the length of the rigid distal section of the new probe has been further reduced to ~35 mm. This paper describes the technical details of the mini-probe and presents experimental results that both quantify the imaging performance and demonstrate its *in vivo* imaging capability, which suggests that it could work as a mini-probe for certain clinical applications.

©2012 Optical Society of America

OCIS codes: (170.3880) Medical and biological imaging; (170.5120) Photoacoustic imaging; (170.2150) Endoscopic imaging.

References and links

1. L. V. Wang, "Prospects of photoacoustic tomography," *Med. Phys.* **35**(12), 5758–5767 (2008).
2. J. M. Yang, K. Maslov, H. C. Yang, Q. Zhou, K. K. Shung, and L. V. Wang, "Photoacoustic endoscopy," *Opt. Lett.* **34**(10), 1591–1593 (2009).
3. A. A. Oraevsky and A. A. Karabutov, "Optoacoustic Tomography," in *Biomedical Photonics Handbook*, T. Vo-Dinh, ed. (CRC Press, 2003).
4. L. V. Wang, "Multiscale photoacoustic microscopy and computed tomography," *Nat. Photonics* **3**(9), 503–509 (2009).
5. C. Li and L. V. Wang, "Photoacoustic tomography and sensing in biomedicine," *Phys. Med. Biol.* **54**(19), R59–R97 (2009).
6. P. Beard, "Biomedical photoacoustic imaging," *Interface Focus* **1**(4), 602–631 (2011).
7. L. V. Wang and S. Hu, "Photoacoustic tomography: in vivo imaging from organelles to organs," *Science* **335**(6075), 1458–1462 (2012).
8. Z. Guo, S. Hu, and L. V. Wang, "Calibration-free absolute quantification of optical absorption coefficients using acoustic spectra in 3D photoacoustic microscopy of biological tissue," *Opt. Lett.* **35**(12), 2067–2069 (2010).
9. C. P. Favazza, L. A. Cornelius, and L. V. Wang, "In vivo functional photoacoustic microscopy of cutaneous microvasculature in human skin," *J. Biomed. Opt.* **16**(2), 026004 (2011).
10. A. Danielli, C. P. Favazza, K. Maslov, and L. V. Wang, "Single-wavelength functional photoacoustic microscopy in biological tissue," *Opt. Lett.* **36**(5), 769–771 (2011).
11. Y. Wang, S. Hu, K. Maslov, Y. Zhang, Y. Xia, and L. V. Wang, "In vivo integrated photoacoustic and confocal microscopy of hemoglobin oxygen saturation and oxygen partial pressure," *Opt. Lett.* **36**(7), 1029–1031 (2011).
12. S. Hu, K. Maslov, and L. V. Wang, "Second-generation optical-resolution photoacoustic microscopy with improved sensitivity and speed," *Opt. Lett.* **36**(7), 1134–1136 (2011).
13. J. Yao, K. I. Maslov, Y. Shi, L. A. Taber, and L. V. Wang, "In vivo photoacoustic imaging of transverse blood flow by using Doppler broadening of bandwidth," *Opt. Lett.* **35**(9), 1419–1421 (2010).
14. J. Yao, K. I. Maslov, Y. Zhang, Y. Xia, and L. V. Wang, "Label-free oxygen-metabolic photoacoustic microscopy in vivo," *J. Biomed. Opt.* **16**(7), 076003 (2011).

15. M. Pramanik and L. V. Wang, "Thermoacoustic and photoacoustic sensing of temperature," *J. Biomed. Opt.* **14**(5), 054024 (2009).
16. M. R. Chatni, J. Yao, A. Danielli, C. P. Favazza, K. I. Maslov, and L. V. Wang, "Functional photoacoustic microscopy of pH," *J. Biomed. Opt.* **16**(10), 100503 (2011).
17. S. Hu and L. V. Wang, "Photoacoustic imaging and characterization of the microvasculature," *J. Biomed. Opt.* **15**(1), 011101 (2010).
18. B. Wang, J. L. Su, A. B. Karpiouk, K. V. Sokolov, R. W. Smalling, and S. Y. Emelianov, "Intravascular photoacoustic imaging," *IEEE J. Quantum Electron.* **16**(3), 588–599 (2010).
19. J. L. Su, B. Wang, and S. Y. Emelianov, "Photoacoustic imaging of coronary artery stents," *Opt. Express* **17**(22), 19894–19901 (2009).
20. A. B. Karpiouk, B. Wang, and S. Y. Emelianov, "Development of a catheter for combined intravascular ultrasound and photoacoustic imaging," *Rev. Sci. Instrum.* **81**(1), 014901 (2010).
21. K. Jansen, A. F. van der Steen, H. M. van Beusekom, J. W. Oosterhuis, and G. van Soest, "Intravascular photoacoustic imaging of human coronary atherosclerosis," *Opt. Lett.* **36**(5), 597–599 (2011).
22. E. Z. Zhang and P. C. Beard, "A miniature all-optical photoacoustic imaging probe," *Proc. SPIE* **7899**, 78991F, 78991F-6 (2011).
23. B. Y. Hsieh, S. L. Chen, T. Ling, L. J. Guo, and P. C. Li, "All-optical scanhead for ultrasound and photoacoustic dual-modality imaging," *Opt. Express* **20**(2), 1588–1596 (2012).
24. B. Wang, A. Karpiouk, D. Yeager, J. Amirian, S. Litovsky, R. Smalling, and S. Emelianov, "Intravascular photoacoustic imaging of lipid in atherosclerotic plaques in the presence of luminal blood," *Opt. Lett.* **37**(7), 1244–1246 (2012).
25. T. J. Allen, A. Hall, A. P. Dhillon, J. S. Owen, and P. C. Beard, "Spectroscopic photoacoustic imaging of lipid-rich plaques in the human aorta in the 740 to 1400 nm wavelength range," *J. Biomed. Opt.* **17**(6), 061209 (2012).
26. Y. Yuan, S. Yang, and D. Xing, "Preclinical photoacoustic imaging endoscope based on acousto-optic coaxial system using ring transducer array," *Opt. Lett.* **35**(13), 2266–2268 (2010).
27. J. M. Yang, C. Favazza, R. Chen, J. Yao, K. Maslov, X. Cai, Q. Zhou, K. K. Shung, and L. V. Wang, "Volumetric photoacoustic endoscopy of upper gastrointestinal tract: ultrasonic transducer technology development," *Proc. SPIE* **7899**, 78990D, 78990D-6 (2011).
28. M. A. Yaseen, S. A. Ermilov, H. P. Brecht, R. Su, A. Conjusteau, M. Fronheiser, B. A. Bell, M. Motamedi, and A. A. Oraevsky, "Optoacoustic imaging of the prostate: development toward image-guided biopsy," *J. Biomed. Opt.* **15**(2), 021310 (2010).
29. X. Wang, W. W. Roberts, P. L. Carson, D. P. Wood, and J. B. Fowlkes, "Photoacoustic tomography: a potential new tool for prostate cancer," *Biomed. Opt. Express* **1**(4), 1117–1126 (2010).
30. C. Sheaff and S. Ashkenazi, "A fiber optic optoacoustic ultrasound sensor for photoacoustic endoscopy," in *Proceedings of IEEE International Ultrasonics Symposium* (Institute of Electrical and Electronics Engineers, San Diego, 2010), pp. 2135–2138.
31. Y. Yang, X. Li, T. Wang, P. D. Kumavor, A. Aguirre, K. K. Shung, Q. Zhou, M. Sanders, M. Brewer, and Q. Zhu, "Integrated optical coherence tomography, ultrasound and photoacoustic imaging for ovarian tissue characterization," *Biomed. Opt. Express* **2**(9), 2551–2561 (2011).
32. C. Dietrich, ed., *Endoscopic Ultrasound: An Introductory Manual and Atlas* (Thieme, New York, 2006).
33. J. Menzel and W. Domschke, "Gastrointestinal miniprobe sonography: the current status," *Am. J. Gastroenterol.* **95**(3), 605–616 (2000).
34. G. J. Tearney, M. E. Brezinski, B. E. Bouma, S. A. Boppart, C. Pitris, J. F. Southern, and J. G. Fujimoto, "In vivo endoscopic optical biopsy with optical coherence tomography," *Science* **276**(5321), 2037–2039 (1997).
35. X. Li, C. Chudoba, T. Ko, C. Pitris, and J. G. Fujimoto, "Imaging needle for optical coherence tomography," *Opt. Lett.* **25**(20), 1520–1522 (2000).
36. X. Liu, M. J. Cobb, Y. Chen, M. B. Kimmey, and X. Li, "Rapid-scanning forward-imaging miniature endoscope for real-time optical coherence tomography," *Opt. Lett.* **29**(15), 1763–1765 (2004).
37. S. H. Yun, G. J. Tearney, B. J. Vakoc, M. Shishkov, W. Y. Oh, A. E. Desjardins, M. J. Suter, R. C. Chan, J. A. Evans, I. K. Jang, N. S. Nishioka, J. F. de Boer, and B. E. Bouma, "Comprehensive volumetric optical microscopy in vivo," *Nat. Med.* **12**(12), 1429–1433 (2007).
38. D. C. Adler, Y. Chen, R. Huber, J. Schmitt, J. Connolly, and J. G. Fujimoto, "Three-dimensional endomicroscopy using optical coherence tomography," *Nat. Photonics* **1**(12), 709–716 (2007).
39. H. Yoo, J. W. Kim, M. Shishkov, E. Namati, T. Morse, R. Shubochkin, J. R. McCarthy, V. Ntziachristos, B. E. Bouma, F. A. Jaffer, and G. J. Tearney, "Intra-arterial catheter for simultaneous microstructural and molecular imaging in vivo," *Nat. Med.* **17**(12), 1680–1684 (2011).
40. A. M. Winkler, P. F. Rice, J. Weichsel, J. M. Watson, M. V. Backer, J. M. Backer, and J. K. Barton, "In vivo, dual-modality OCT/LIF imaging using a novel VEGF receptor-targeted NIR fluorescent probe in the AOM-treated mouse model," *Mol. Imaging Biol.* **13**(6), 1173–1182 (2011).
41. R. Kiesslich, J. Burg, M. Vieth, J. Gnaendiger, M. Enders, P. Delaney, A. Polglase, W. McLaren, D. Janell, S. Thomas, B. Nafe, P. R. Galle, and M. F. Neurath, "Confocal laser endoscopy for diagnosing intraepithelial neoplasias and colorectal cancer in vivo," *Gastroenterology* **127**(3), 706–713 (2004).
42. P. Kim, E. Chung, H. Yamashita, K. E. Hung, A. Mizoguchi, R. Kucherlapati, D. Fukumura, R. K. Jain, and S. H. Yun, "In vivo wide-area cellular imaging by side-view endomicroscopy," *Nat. Methods* **7**(4), 303–305 (2010).

43. L. Qiu, D. K. Pleskow, R. Chuttani, E. Vitkin, J. Leyden, N. Ozden, S. Itani, L. Guo, A. Sacks, J. D. Goldsmith, M. D. Modell, E. B. Hanlon, I. Itzkan, and L. T. Perelman, "Multispectral scanning during endoscopy guides biopsy of dysplasia in Barrett's esophagus," *Nat. Med.* **16**(5), 603–606, 1p, 606 (2010).
44. N. G. Terry, Y. Zhu, M. T. Rinehart, W. J. Brown, S. C. Gebhart, S. Bright, E. Carretta, C. G. Ziefle, M. Panjehpour, J. Galanko, R. D. Madanick, E. S. Dellon, D. Trembath, A. Bennett, J. R. Goldblum, B. F. Overholt, J. T. Woosley, N. J. Shaheen, and A. Wax, "Detection of dysplasia in Barrett's esophagus with in vivo depth-resolved nuclear morphology measurements," *Gastroenterology* **140**(1), 42–50 (2011).
45. J. M. Yang, C. Favazza, R. Chen, J. Yao, X. Cai, K. Maslov, Q. Zhou, K. K. Shung, and L. V. Wang, "Simultaneous functional photoacoustic and ultrasonic endoscopy of internal organs in vivo," *Nat. Med.* **18**(8), 1297–1302 (2012).
46. Q. Zhou, X. Xu, E. J. Gottlieb, L. Sun, J. M. Cannata, H. Ameri, M. S. Humayun, P. Han, and K. K. Shung, "PMN-PT single crystal, high-frequency ultrasonic needle transducers for pulsed-wave Doppler application," *IEEE Trans. Ultrason. Ferroelectr. Freq. Control* **54**(3), 668–675 (2007).
47. Laser Institute of America, *American National Standard for Safe Use of Lasers*, ANSI Z136.1–2007 (American National Standards Institute, Inc., New York, NY, 2007).

1. Introduction

Photoacoustic endoscopy (PAE) [1, 2] is a novel imaging technique that embodies photoacoustic tomography (PAT) [1, 3–7] in a small probe to image internal organs through intracavitary introduction. PAT is similar to conventional ultrasound imaging, since its image rendering is predicated on the same ultrasound signal detection. Such similarities engender PAT's virtually seamless compatibility with traditional ultrasound imaging. Development of an integrated photoacoustic (PA) and ultrasonic (US) "mini-probe" for use in an instrument channel of a conventional video endoscope is an important strategy to realize the clinical benefits of dual modality (PA and US) imaging. Ultrasound image contrast relies on bulk mechanical properties of tissue, providing limited functional information, whereas PAT's spectroscopic imaging capability provides a wealth of physiological or functional information, including hemoglobin concentration, oxygen saturation of hemoglobin [8–12], velocity of blood flow [13, 14], temperature [15], pH [16], etc. Due to these benefits, PAE [1, 2] and other minimally invasive imaging techniques based on PAT [6, 17, 18] have been intensely developed for applications in such clinical areas as the cardiovascular [18–25], gastrointestinal [2, 26, 27], and urogenital [28–31] systems. These techniques are expected to provide a useful complement to other endoscopic modalities, such as endoscopic ultrasound (EUS) [32, 33], endoscopic optical coherence tomography (OCT) [34–40], confocal endoscopy [41, 42], and endoscopic polarized scanning spectroscopy [43, 44].

Previously, we reported a PA endoscopic probe that employs a scanning mirror and built-in actuator and was developed for gastrointestinal tract imaging applications [2, 27, 45]. The reported probe was 3.8 mm in diameter and ~38 mm long, and it enabled simultaneous PA and US imaging via the single device [45]. However, a 3.8 mm diameter was too large to fit in the instrument channel (typically ~2.8 mm or ~3.7 mm diameter) of a standard video endoscope, and thus newer generation probes should be further miniaturized. Here we report technical advancements that have led to a much smaller probe diameter of 2.5 mm and an ~35 mm rigid length (distal end of the endoscope). Importantly, to achieve adequate signal sensitivity within the available aperture size, we designed and engineered a focused US transducer using lead magnesium niobate-lead titanate (PMN-PT) [46]. This new mini-probe can be inserted into the instrument channel of a standard video endoscope and be used with the guidance of the video endoscope. Moreover, it also permits simultaneous PAE and EUS imaging that provides complementary contrast. To our knowledge, this is the smallest diameter, fully encapsulated probe among all reported PA endoscopic probes that can be utilized for *in vivo* imaging. Other smaller photoacoustic endoscopy probes are not fully encapsulated and/or have not demonstrated *in vivo* imaging capabilities. Here, we describe technical details of the implemented US transducer and endoscopic probe, and present experimental results which quantify the endoscope's imaging performance and demonstrate its *in vivo* imaging ability. Also, we discuss its specific use in the instrument channel of a standard video endoscope.

2. Materials and methods

2.1 Integrated 2.5-mm outer diameter PA-US endoscopic mini-probe

The implemented endoscopic probe has a ~2 m long flexible section and a ~35 mm long rigid distal section, where the scanning device is located. A photograph and a schematic diagram of the probe's rigid distal end are presented in Figs. 1(a) and 1(b), respectively. The distal section has a streamlined structure with a dome shaped end for smooth intracavitary advancement, and is sheathed with biocompatible stainless steel and polyethylene terephthalate (PET) plastic tubes. The endoscopic probe is comprised of three key units: an optical fiber and US transducer unit [Fig. 1(c)], a scanning mirror unit [Fig. 1(d)], and a micromotor unit [Fig. 1(e)].

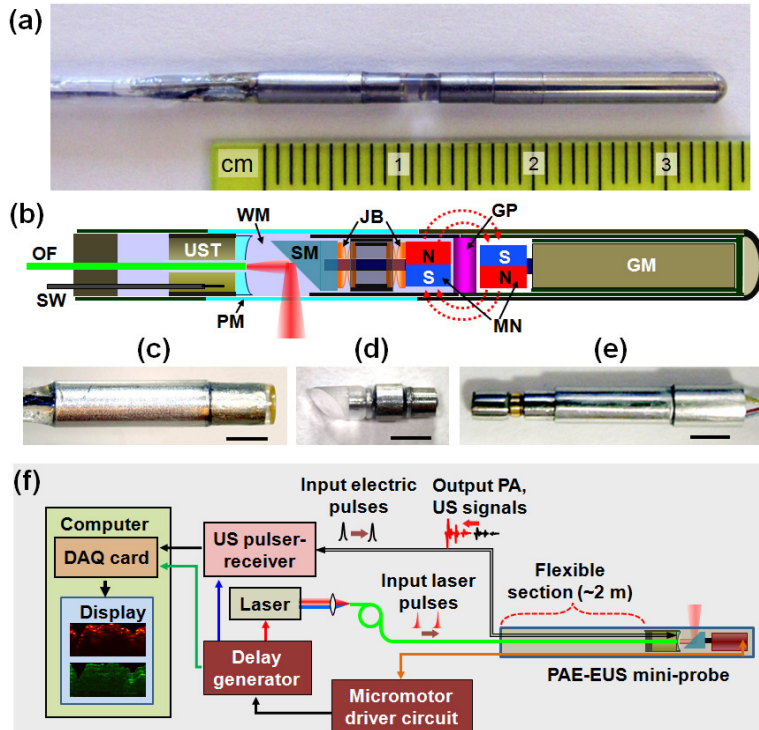


Fig. 1. (a) Photo of the integrated PAE-EUS mini-probe's rigid distal end (2.5 mm diameter and ~35 mm length). (b) Schematic of the mini-probe. GM, geared micromotor; GP, glass partition; JB, jewel bearings; MN, magnets; OF, optical fiber; PM, plastic membrane (imaging window); SM, scanning mirror; SW, signal wire; UST, ultrasonic transducer; WM, water medium. (c) Optical fiber and US transducer unit. (d) Scanning mirror unit. (e) Micromotor unit. In (c)–(d), the scale bars represent 2 mm. (f) Block diagram showing the peripheral systems of the mini-probe.

A single strand of multimode optical fiber (0.22 NA, 365 μm core diameter, BFL22-365, Thorlabs) delivers laser pulses for PA imaging, and a ring-shaped focused US transducer detects both PA and US pulse-echo signals. The optical fiber and US transducer are coaxially aligned so that the optical illumination and acoustic detection overlap to optimize the sensitivity. A mechanically rotated, dielectric-coated fused silica mirror (BB05-E02, Thorlabs) with a 45°-deflected reflection surface serves as the principle component of the scanning mechanism (referred to as a scanning mirror). The mirror reflects both the laser light and acoustic waves, and performs rotational scanning at a B-scan frame of ~4 Hz, driven by a geared micromotor (SBL015-06XXPG254, Namiki Precision). A liquid medium (de-ionized water) fills the sealed inner cavity of the endoscope and provides acoustic coupling between

the probe's imaging window and the transducer. However, to provide an in-air working environment, the micromotor is physically isolated from the liquid medium. The torque required to rotate the mirror is transferred through magnetic coupling of the mirror and the micromotor.

All metal frames that secure the three key units [Figs. 1(c)–1(e)] are constructed from stainless steel or brass. However, the imaging window is formed from an optically and acoustically transparent plastic tube with a wall thickness of $\sim 70\ \mu\text{m}$. The rigid stainless steel housing is sheathed with another PET tube ($\sim 25\ \mu\text{m}$ thickness) to fix the micromotor's four electric wires ($\sim 200\ \mu\text{m}$ thickness for each wire). The endoscope's angular field-of-view is partially blocked by the electric wires; however, it covers $\sim 310^\circ$. Another PET tube encloses all of the wires (optical fiber, US transducer's signal wire, and the motor wires) over the 2-m long, flexible section.

Figure 1(f) shows the peripheral systems, composed of a micromotor driver circuit, a delay generator, a laser system, a US pulser-receiver including an amplifier, a data acquisition (DAQ) card, and a computer for recording signals and displaying images. For PA imaging, laser pulses (584 nm, ~ 10 ns pulse width) from a tunable dye laser (Cobra HRR, Sirah), pumped by a solid-state, diode-pumped Nd:YLF laser (INNOSLAB IS811-E, EdgeWave), are guided by the optical fiber and emitted through the central hole of the US transducer. After exiting the fiber, the laser beams are then directed by the scanning mirror towards the tissue to generate PA waves. The PA waves that propagate to the scanning mirror are reflected by the same mirror, sent to the US transducer, converted into electrical signals, amplified by the US pulser-receiver (5072PR, Panametrics), and digitally recorded by the DAQ card (NI PCI-5124, National Instruments). In the US pulse-echo imaging mode, electric pulses generated by the US pulser-receiver are sent to the US transducer, which converts the electric pulses to acoustic pulses, and the US transducer captures reflected acoustic waves as in conventional US imaging.

The micromotor has a three-stage gear head with a gear ratio of 254 to 1. It communicates with the driver circuit via the four electric wires; two wires supply a DC voltage, one wire controls the direction, and the fourth wire transmits the motor's angular position-encoded signal to the driver circuit. For each full rotation of the motor, the motor's shaft and the scanning mirror rotate by $\sim 1.42^\circ$ and the driver circuit generates a corresponding TTL signal. The driver circuit's voltage was kept at a constant value of ~ 3.2 V, and the resulting rotational speed of the scanning mirror was ~ 4 Hz. Since we utilized the TTL signal to trigger each subsystem with a different time delay produced by the delay generator, all sequences were synchronized by this TTL signal.

Every 1.42° of the mirror's constant rotation, we excite and acquire PA and US A-line signals alternately, with each signal offset by $\sim 30\ \mu\text{s}$ from the previous signal. This time delay ensures that consecutive signals will not interfere with each other. However, this delay does not significantly affect co-registration of the two images because the difference between the angular positions of each signal is small and is well within the spatial resolution of the US transducer. Due to the large ratio of sound propagation speeds in water and glass (1.5/5.1, longitudinal wave; 1.5/3.3, shear wave), the scanning mirror exhibits total internal acoustic reflection within the acceptance angles of the US transducer and inserts no additional propagation losses into the US detection.

2.2 PMN-PT focused ultrasonic transducer

The US transducer determines the spatial resolution for both PA and US imaging. Considering the endoscope's outer diameter and housing thickness, we limited the diameter for the US transducer's piezoelectric-element to ~ 2 mm. To achieve adequate signal sensitivity and high spatial resolution with the restricted element size, we fabricated a focused US transducer using highly sensitive PMN-PT single crystal as a piezoelectric-material, which has highest longitudinal coupling coefficients (k_{33}) $>90\%$, and targeted a center

frequency of around 40 MHz. Figures 2(a) and 2(b) show a schematic diagram and photo of the implemented US transducer, respectively. The piezo-element has an outer diameter of ~1.8 mm and an inner hole diameter of ~0.5 mm, and its front and back electrodes were formed by sputtering chrome and gold, and electrically connected to the transducer housing (ground) and a backing material (E-Solder 3022, VonRoll Isola, New Haven, CT), respectively. The backing material acts as a support and an acoustic damper, and is connected to the core wire of a 0.44-mm thick, 50-Ω coaxial cable (its shield wires are connected to the housing). On the front electrode, conductive silver epoxy was formed as an acoustic matching layer to provide more efficient acoustic signal transmission.

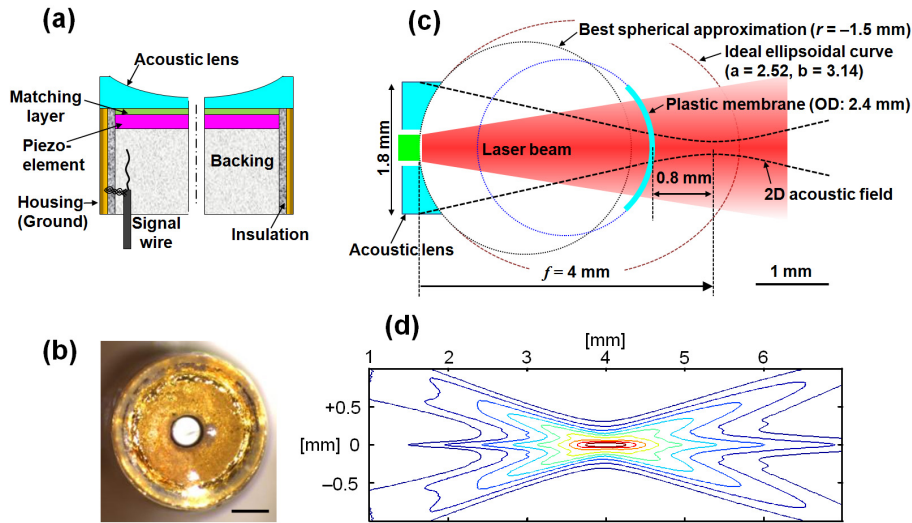


Fig. 2. (a) Schematic of the PMN-PT focused US transducer. (b) Front view of the implemented US transducer, showing the optical fiber located at the center. Scale bar, 500 μm . (c) Diagram showing the dimensions of the plastic acoustic lens, membrane position, and targeted working distance. (d) Simulated two-dimensional (2D) transmission acoustic field of the focused US transducer. The -6dB beam diameter at the 4-mm focal distance is $\sim 80 \mu\text{m}$. The vertical and horizontal axes represent transverse and radial (axial) distances from the US transducer.

The acoustic focusing was achieved by attaching a plano-concave plastic acoustic lens to the flat surface of the US transducer. The plastic acoustic lens was fabricated in-house by molding polyester resin. In the case of plano-concave-shaped acoustic lens shown in Fig. 2(a), the concave surface's ideal curve without geometric acoustic aberration is expressed by an ellipsoid shape with a shorter half axis length of $a \equiv f \sqrt{(n-1)/(n+1)}$ and a longer half axis length of $b \equiv f \cdot n / (n+1)$ [27]. Here, f is the focal length, and the focal point is located on the longer axis: the acoustic focal point is not located at either of the mathematical foci of the ellipsoid. Also, n is the acoustic speed ratio of the solid lens to the surrounding liquid medium (water in this study). Considering the endoscope's dimensions and working distance, we targeted a focal distance of ~ 4 mm (acoustic NA = 0.22) for the transducer. For this distance, the formulas yield the values of $a = 2.52$ mm and $b = 3.14$ mm, for the given acoustic speed ratio ($n = 1.68$) between the plastic lens and water medium. In the actual lens fabrication, however, we formed the front surface with a spherical shape that has a radius of curvature (r) of ~ 1.5 mm. The radius of curvature was determined by the spherical curve fitting method shown in Fig. 2(c), targeting the 4 mm focal length. To minimize the acoustic attenuation of high frequency acoustic waves, we chose the edge and center thickness of the acoustic lens to be as thin as possible, ~ 0.4 mm and ~ 0.1 mm, respectively.

In Fig. 2(c), several important geometric parameters of the focused US transducer and endoscope are schematically displayed. As shown in the figure, no light focusing optics are coupled with the optical fiber to broadly illuminate the target tissue; the laser beam diverges with a full angle of $\sim 20^\circ$ in the aqueous medium. Since the plastic membrane is located ~ 3.2 mm apart from the lens surface, the laser beams' spot size is ~ 1.5 mm in diameter when it passes through the imaging window. We set the laser power at ~ 0.04 mJ/pulse, which yields an optical fluence of ~ 2.3 mJ/cm² ($\sim 12\%$ of the ANSI safety limit [47] for allowable skin laser fluence) at the plastic membrane. In designing the endoscope, we targeted the working distance of ~ 0.8 mm from the endoscope's surface to image gastrointestinal diseases, such as Barrett's esophagus or colorectal tumors, which develop in the epithelial layer of the lumen. Moreover, we designed the mini-probe to operate in direct contact with the target's surface. Based on the described parameters, we simulated the implemented focused US transducer's two-dimensional transmission acoustic field with an acoustics modeling software package (Field II), and we present the results in Fig. 2(d).

2.3 *In vivo* animal imaging experiment

To demonstrate the integrated mini-probe's *in vivo* imaging capability, we imaged the descending colon of an adult Sprague Dawley rat (~ 450 g; Harlan National Customer Service Center). The rat was fasted for ~ 12 hr before the experiment, to increase the likelihood of an empty colon for imaging. In the experiment, the animal was anesthetized with isoflurane (4% for induction), and a cocktail of 87 mg/kg ketamine and 13 mg/kg xylazine was administered (IP) to provide time to prepare and mount the animal. Once the animal was properly positioned, medical ultrasound gel was inserted into the descending colon via a small plastic tube. The ultrasound gel provided acoustic coupling between the tissue and US transducer, and also lubricated the probe during colon insertion through the anus. Then, we inserted the endoscopic probe into the colon ~ 5 cm deep from the animal's anus and performed pullback volumetric scans over a ~ 4 cm range during constant pullback translation of the probe at a speed of ~ 160 μ m/s. About 1000 cross-sectional or B-scan slices with a longitudinal spacing of ~ 40 μ m were acquired for each imaging mode. During imaging, anesthesia was maintained with 1.5–2.0% isoflurane supplied through a nose cone. After the experiment, the rat was euthanized by a pentobarbital overdose (150 mg/kg, IP). All procedures in the experiment followed the protocol approved by the Institutional Animal Care and Use Committee at Washington University in St. Louis.

3. Results and discussion

Several of the focused US transducer's operating parameters were quantified, including the center frequency, bandwidth, and resolution. First, we measured the focal distance of the US transducer by finding the distance which generated the maximum echo signal from a quartz block. The maximum signal was observed at a distance of ~ 4.1 mm from the transducer surface, close to the originally targeted 4-mm focal distance shown in Fig. 2(c). At this position, we recorded the time-domain signal and analyzed the waveform to determine the center frequency and frequency bandwidth. Figures 3(a) and 3(b) show the recorded time-domain signal and acoustic frequency distribution (processed from fast Fourier analysis), respectively. Based on the -6 dB width of the frequency distribution [Fig. 3(b)], we determined the center frequency to be ~ 33 MHz, with a bandwidth of ~ 20 MHz (60% fractional bandwidth). Prior to attaching the acoustic lens, we similarly measured the original center frequency and fractional bandwidth of the US transducer, which were ~ 38 MHz and 43%, respectively. We speculate that the frequency shift and fractional bandwidth increase were caused by the formation of the plastic acoustic lens.

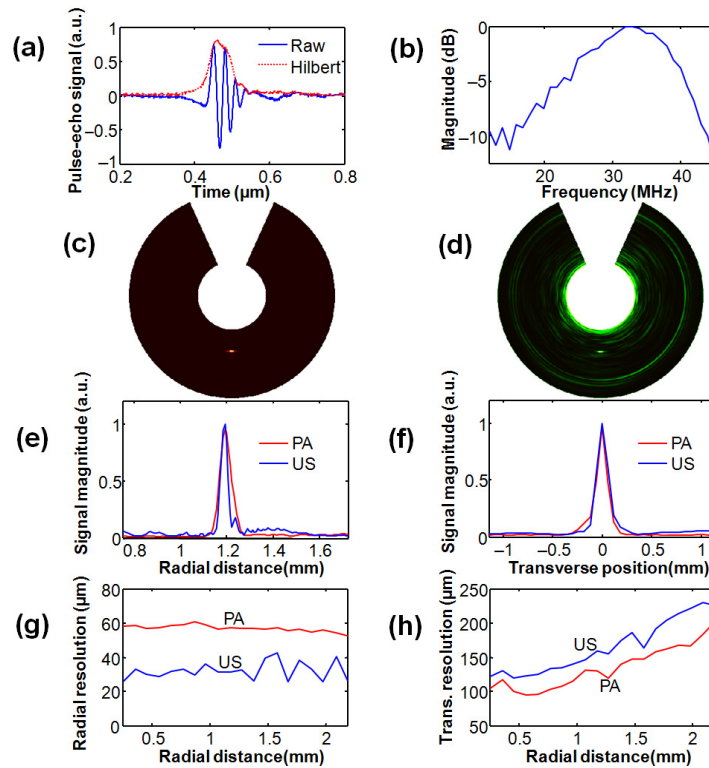


Fig. 3. (a) Typical US pulse-echo A-line signal of a tungsten wire: raw data and Hilbert-transformed or enveloped signal. (b) Acoustic frequency distribution of the waveform shown in (a). (c, d) PA and US B-scan images of a 20- μm thick tungsten wire. (e) PA and US radial point-spread-functions (PSFs) of the tungsten wire. (f) PA and US transverse PSFs of the tungsten wire. (g) Radial resolution vs. target distance. (h) Transverse resolution vs. target distance.

The endoscopic probe's spatial resolution was also quantified by imaging a $\sim 20 \mu\text{m}$ thick tungsten wire at different locations. Figures 3(c) and 3(d) show representative PA and US B-scan images of the tungsten wire, from which we determined the point spread functions (PSFs) and hence spatial resolutions of the two imaging modalities. To more accurately quantify the resolution, we averaged 200 B-scans acquired at the same position. Figures 3(e) and 3(f) represent the radial and transverse PSFs of the target shown in Figs. 3(c) and 3(d). By analyzing -6 dB widths (i.e., FWHM) of the PSFs, we determined the radial and transverse resolutions, and the resolution dependencies on the target distance from the surface of the probe are plotted in Figs. 3(g) and 3(h), respectively. As presented in Fig. 3(g), the PA and US radial resolutions show relatively constant values, $\sim 58 \mu\text{m}$ for PA and $\sim 30 \mu\text{m}$ for US, over the measured ranges. However, the transverse resolutions show strong target distance dependence [Fig. 3(h)]; the PA and US transverse resolutions show minimum values of $\sim 100 \mu\text{m}$ and $\sim 120 \mu\text{m}$, respectively, at $\sim 0.5 \text{ mm}$ distance from the endoscope's surface, corresponding to $\sim 4.1 \text{ mm}$ from the transducer's surface, and gradually increase according to the target distance.

In theory, the US transverse resolution is finer than that of PA in the focal zone because both transmission and receiving in US imaging contribute to resolution. However, the experimental result showed an opposite relationship (i.e., the measured PA transverse resolution was better than the measured US transverse resolution). Also, the experimentally measured -6 dB US transverse resolution of $120 \mu\text{m}$ was much worse than that of the simulated result ($\sim 80 \mu\text{m}$) shown in Fig. 2(d). We speculate that these results were caused by

the presence of the 70- μm thick plastic membrane, which distorts the acoustic waves and more greatly impacts the US imaging mode, because it requires round-trip propagation of the acoustic waves through the membrane. The strong reverberation signals generated by the plastic membrane are clearly seen in the US pulse-echo imaging mode [Fig. 3(d)] and represent such membrane effect. The measured 0.5 mm working distance [Fig. 3(h)] was different from our expectation (design) shown in Fig. 2(c), likely due to the imperfect placement of the focused transducer inside the probe housing.

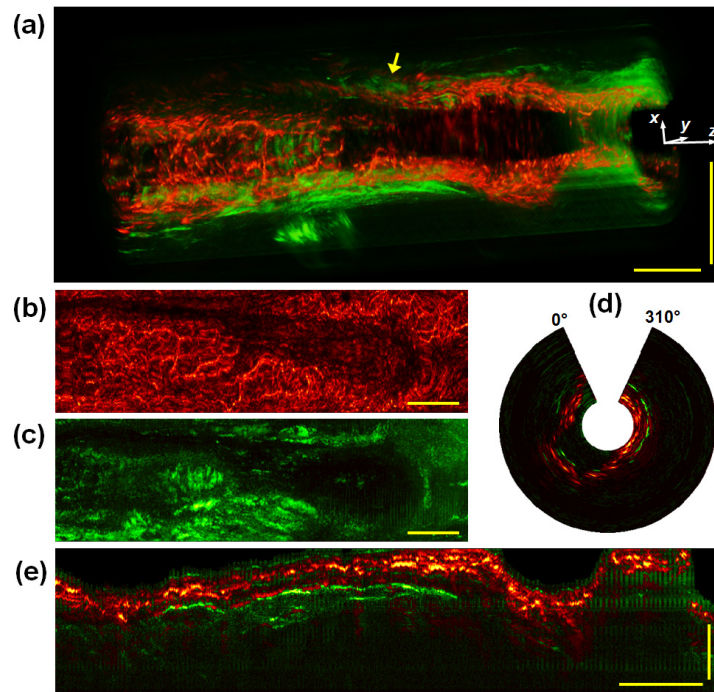


Fig. 4. (a) Three-dimensionally-rendered PAE-EUS structural image from a rat colon acquired *in vivo* over a 4 cm range with a 10 mm image diameter (3.7 mm radial imaging depth). The right-hand side (+ z axis) and lower portion ($-y$ axis) of the image correspond to the anus and the ventral side of the animal, respectively. The horizontal and vertical scale bars represent 5 mm. (b, c) PA and US radial-maximum amplitude projection images of (a). The vertical axis corresponds to the angular field-of-view, covering $\sim 310^\circ$, and the horizontal axis corresponds to the pullback length of 4 cm. Scale bars represent 5 mm (only for the horizontal direction). (d) A representative x - y slice near the location indicated by the arrow in (a). (e) A longitudinal slice of the image volume of (a). All the PA and US signals are mapped on a linear scale, and the horizontal and vertical scale bars represent 5 mm and 1 mm, respectively.

In Fig. 4(a), we present a co-registered PA and US three-dimensional image from the rat colon acquired *in vivo*. The image was processed from a volumetric data set covering a 4 cm long cylindrical volume with a 10 mm diameter (i.e., ~ 3.7 mm radial imaging depth), which required a scanning time of ~ 4 min at the 4 Hz frame rate. The PA structural image was created from PA data acquired at 584 nm, where the PA signal is dependent on the total hemoglobin concentration only. The volume-rendered PA image shows the vasculature in and near the colon wall, while the US image reveals the density distribution of the tissues. To illustrate the image contrast difference between the two imaging modes in a two-dimensional plane, we produced PA and US radial-maximum amplitude projection images from the volumetric image Fig. 4(a) and present them in Figs. 4(b) and 4(c), respectively. A representative B-scan slice and longitudinal slice are shown in Figs. 4(d) and 4(e), respectively, where the US image shows clear contrast at the boundary of the colon wall and the PA image shows contrast originating from the vasculature in the wall. Additionally, as

shown in Fig. 4(e), a periodic oscillation of ~ 0.6 Hz was observed, which was attributed to the respiratory motion of the animal.

These experimental results demonstrate the 2.5-mm diameter integrated PAE-EUS mini-probe's *in vivo* imaging capability and suggest that the 1.8-mm aperture focused US transducer possesses adequate PA signal sensitivity at an optical fluence level of $\sim 12\%$ of the ANSI safety limit (for skin exposure). The implemented 2.5 mm diameter includes the entire outer sheath and has a size comparable to existing EUS mini-probes [33] manufactured for clinical use in the 2.8-mm instrument channel. For clinical use in the instrument channel of a video endoscope, however, the 35 mm-long rigid distal section should be further shortened so that it can pass the sharply bent section located near the entrance of the instrument channel. Currently, the probe must be inserted through the exit port of the endoscope to avoid this bend. The length-wise miniaturization of the rigid distal end of the endoscope was limited by the mechanical section that includes the 12-mm long commercial micromotor. The micromotor in this section was not optimally designed for this probe configuration. Development of a smaller actuator optimized for this endoscopic configuration would make it more compatible for use as a mini-probe in a standard instrument channel.

The current mini-probe could be more readily incorporated into a 3.7-mm diameter instrument channel (Fig. 5), which provides more space and bending radius than the 2.8-mm instrument channel, and future studies will target this strategy for human imaging. Several organs, such as the descending colon or uterus, which do not require sharp bends of the probe, could be imaged with this method.

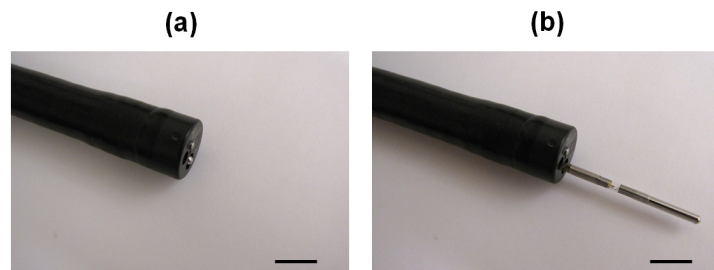


Fig. 5. Photos of the mini-probe positioned fully within (a) and projecting from (b) the 3.7-mm instrument channel of a video endoscope. The scale bars represent 1 cm.

4. Conclusion

We have successfully implemented a 2.5-mm diameter integrated PAE-EUS mini-probe, and demonstrated its *in vivo* imaging capability. The probe's diameter is 1.5 times smaller than our previous endoscopic probe and less than the 2.8-mm diameter instrument channel of existing standard video endoscopes. The endoscope can produce co-registered PA and US images of internal organs simultaneously at a frame rate of ~ 4 Hz for each imaging mode. Due to the probe's long and rigid distal end, its true mini-endoscopic compatibility is partially limited by the sharply-bent entrance section of the instrument channel in a standard video endoscope. However, the mini probe can be incorporated in the 3.7-mm instrument channel and used for some clinical applications.

Acknowledgments

We thank Prof. James Ballard for his attentive reading of the manuscript, and Dr. Konstantin Maslov for useful discussions. This work was sponsored in part by National Institutes of Health grants R01 CA157277, R01 EB000712, R01 EB008085, R01 CA134539, U54 CA136398, R01 CA159959, and P41 EB002182. L.W. has a financial interest in Microphotoacoustics, Inc. and Endra, Inc., which, however, did not support this work. J.-M.Y. was supported in part by a Korea Research Foundation Grant funded by the Korean Government (KRF-2007-357-C00039).